

Tidal Evolution and Spin-Orbit Dynamics: The Critical Role of Rheology.

Clodoaldo Ragazzo · Lucas Ruiz dos Santos

the date of receipt and acceptance should be inserted later

Abstract This study analyzes secular dynamics using averaged equations that detail tidal effects on the motion of two extended bodies in Keplerian orbits. It introduces formulas for energy dissipation within each body of a binary system. The equations, particularly in contexts like the Sun-Mercury system, can be delineated into a fast-slow system. A significant contribution of this work is the demonstration of the crucial role complex rheological models play in the capture by spin-orbit resonances. This is particularly evident in the notable enlargement of the basin of attraction for Mercury's current state when transitioning from a single characteristic time rheology to a dual characteristic time model, under the constraint that both models comply with the same estimate of the complex Love number at orbital frequency. The study also underscores the importance of Mercury's elastic rigidity on secular timescales.

1 Introduction

Newton formulated the law of gravitation and concluded that the motion of the centers of mass of spherical bodies is equivalent to that of point masses. The solution to the resulting two-body problem, as obtained by Newton, forms the backbone of all subsequent developments in celestial mechanics. Notably, while planets and major satellites are almost spherical, even slight deformations

C. Ragazzo (ORCID 0000-0002-4277-4173)
Instituto de Matemática e Estatística, Universidade de São Paulo, 05508-090 São Paulo, SP, Brazil
E-mail: ragazzo@usp.br
Partially supported by FAPESP grant 2016/25053-8.

L. S. Ruiz (ORCID 0000-0002-5705-5278)
Instituto de Matemática e Computação, Universidade Federal de Itajubá, 37500-903 Itajubá, MG, Brazil
E-mail: lucasruiz@unifei.edu.br

caused by spin and tidal forces can significantly influence their rotation and orbits.

Building on the foundational works of Newton, Laplace, Thomson, Darwin, and others, a significant advancement in understanding tidal effects on celestial motion was made by Kaula [Kaula \(1964\)](#), who decomposed tidal forces harmonically in space and time for two bodies in a Keplerian orbit, using Love numbers to evaluate changes in orbital elements. Recent updates to Kaula's theory are available in [Boué and Efroimsky \(2019\)](#), with additional insights in [Efroimsky \(2012\)](#). Over the last 70 years, extensive research has focused on these tidal effects. Notable contributions include Ferraz-Mello's [Ferraz-Mello \(2013\)](#) model, which builds on Darwin's theory with non-spherical hydrostatic states, detailed further in [Folonier et al. \(2018\)](#), [Ferraz-Mello et al. \(2020\)](#), and summarized in [Ferraz-Mello \(2019\)](#), [Ferraz-Mello \(2021\)](#). Various studies, including those by [Goldreich \(1966\)](#), [Singer \(1968\)](#), [Alexander \(1973\)](#), [Mignard \(1979\)](#), [Hut \(1981\)](#), [Makarov and Efroimsky \(2013\)](#), [Correia et al. \(2014\)](#), [Ferraz-Mello \(2015\)](#), and [Boué et al. \(2016\)](#), have explored deformation equations averaged over orbital motion, particularly in low and high-viscosity scenarios. The averaged equations used in this work are identical to those presented in [Correia and Valente \(2022\)](#).

In this paper we study the secular-planar dynamics of two extended bodies. We make the following assumptions:

- 1) The two bodies are deformable, nearly spherical at all times;
- 2) The spins (or rotation vectors) of the deformable bodies remain perpendicular to the orbital plane.
- 3) The bodies are: radially stratified, each body layer is homogeneous and has a linear visco-elastic rheology, see e.g. [Sabadini et al. \(2016\)](#). Fluid layers, if present, must be sufficiently coupled to the adjacent layers such that the rotation of each layer remains close to the average rotation of the body.

In this paper, we crucially use that, from the perspective of gravitation, the rheology of a body with a finite number of homogeneous layers is equivalent to that of a homogeneous body with a sufficiently more complex rheology [Gevorgyan et al. \(2023\)](#).

The aim of this study is to analyze the secular dynamics arising from the averaged equations. The primary novelty of this work lies in demonstrating the importance of using complex rheological models in the capture by spin-orbit resonances. More specifically, it highlights the significant enlargement of the basin of attraction of Mercury's current state when transitioning from a rheology with one characteristic time to one with two characteristic times. Both rheologies are constrained to satisfy the same estimate of the complex Love number at orbital frequency.

In the next section, we present the main results of the paper. The final section provides several mathematical details involved in deriving these results.

2 Main results.

The foundational equations for the orbit and rotation of an extended body are well-established in the literature. Various equations detailing the deformation of extended bodies exist. In a companion paper [Ragazzo and Ruiz \(2024\)](#), we averaged the equations provided in [Ragazzo and Ruiz \(2017\)](#) with respect to the orbital motion, excluding the term accounting for the inertia of deformations as discussed in [Correia et al. \(2018\)](#). These equations are applicable to any rheological model. We obtained essentially the same averaged equations as those presented in [Correia and Valente \(2022\)](#). The only difference is the inclusion of a centrifugal deformation term, which is not relevant in the planar case. It is important to emphasize that the averaged equations in [Correia and Valente \(2022\)](#) are more general as they do not necessitate the spins of the bodies to be perpendicular to the orbital plane.

Let m_α and m represent the masses of two celestial bodies, which could be a planet and a star, or a planet and a satellite, etc. We name the bodies such that the “ α body” is the largest $m_\alpha \geq m$. The quantities of the large body will always be labeled with an index α and those of the small body will have no label.

We assume that both bodies are almost spherical, deformable, and the deformations are volume preserving. In this situation the mean moments of inertia, denoted as I_o and $I_{o\alpha}$, remain constant in time, a result attributed to Darwin [Rochester and Smylie \(1974\)](#).

The motion of the two-body system is determined by three sets of equations: the equations for the relative positions of the centers of mass (orbit), the equations for the rotation of each body about their centers of mass (spin), and the equations for the deformation of each body. In [Section 3.1](#), we present these fundamental equations.

2.1 Rheology and Love numbers

The rheology of a body determines the Love number $k_2(\sigma)$, where σ is the angular frequency of the tidal raising force. For a stratified body with a finite number of homogeneous layers, the Love number can be written as [Sabadini et al. \(2016\)](#) (see also [Gevorgyan et al. \(2023\)](#) and [Gevorgyan \(2021\)](#)):

$$k_2(\sigma) = k_\infty + (k_o - k_\infty) \left(\frac{h_1}{1 + i\tau_1\sigma} + \dots + \frac{h_{n+1}}{1 + i\tau_{n+1}\sigma} \right). \quad (2.1)$$

In these equations:

- $k_\infty := \lim_{\sigma \rightarrow \infty} k_2(\sigma)$ is the asymptotic value of the Love number at high frequencies.
- $k_o := k_2(0)$ is the Love number at frequency zero, also called secular Love number ¹.

¹ The softest possible body is one composed of a perfect fluid, which is held together solely by self-gravity. In this case, $k_o = k_f$, where k_f is the fluid Love number. Let R be the body

- τ_i is the i^{th} characteristic time of the rheology.
- $h_i > 0$ is the relative amplitude of the i^{th} mode of the rheology, which is associated to the characteristic time τ_i . The relative amplitudes add to one:

$$h_1 + h_2 + \dots + h_{n+1} = 1.$$

As discussed in [Gevorgyan et al. \(2023\)](#), the Love number in equation (2.1) corresponds to that of a homogeneous body with a generalized Voigt rheology, the spring-dashpot representation of which is given in Figure 1.

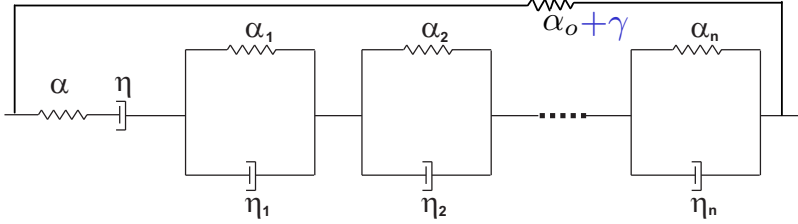


Fig. 1: The generalized Voigt model. The constant γ (blue) represents self-gravity rigidity.

All the simple rheological models used in the literature, such as: Maxwell, Kelvin-Voigt, Standard Anelastic Solid (SAS), Burgers, Bland's generalized Voigt (Figure 2 LEFT), and Bland's generalized Maxwell (Figure 2 RIGHT); are particular cases of the generalized Voigt rheology depicted in Figure 1. The Andrade model can be approximated with arbitrary precision by a generalized Voigt model, as demonstrated in [Gevorgyan et al. \(2020\)](#).

2.2 Passive deformation.

The moment of inertia matrix \mathbf{I} of a body in an inertial reference frame can be written as:

$$\mathbf{I} = \mathbf{I}_o(\mathbf{1} - \mathbf{b}). \quad (2.3)$$

volumetric radius and R_I be the radius of inertia, defined as the radius of a homogeneous sphere of mass m and moment of inertia \mathbf{I}_o . Assuming that the density is non-decreasing towards the center, the following approximation (valid for $0.2 < \frac{\mathbf{I}_o}{mR^2} \leq 0.4$) holds ([Ragazzo, 2020](#), Eqs. 1.2 and 1.8, Theorems 4.1 and 4.2):

$$k_f \approx \frac{3}{2} \left(\frac{R_I}{R} \right)^5 \quad \text{where:} \quad R_I^2 := \frac{5}{2} \frac{\mathbf{I}_o}{m}. \quad (2.2)$$

The maximum value of R_I/R is one, achieved in a homogeneous body, for which $k_f = \frac{3}{2}$. The approximation in equation (2.2) was also proposed in [Consozzi et al. \(2023\)](#).

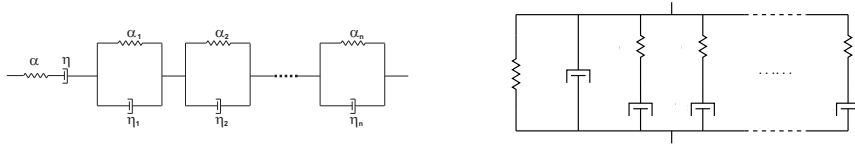


Fig. 2: LEFT: Generalized Voigt model in Bland (1960) Figure 1.8. RIGHT: Generalized Maxwell model Bland (1960) Figure 1.9.

where $\mathbf{1}$ is the identity and \mathbf{b} is a symmetric and traceless matrix. We denote matrices and vectors in bold face. The matrix \mathbf{b} is termed the deformation matrix. The deformation matrix of the α -body is denoted as \mathbf{b}_α .

Since the bodies are nearly spherical and tidal deformations are minor, the variations in orbital elements occur gradually. As a result, the tidal forces can be approximated by those of point masses undergoing Keplerian motion. Within this framework, tidal forces can be harmonically decomposed both temporally, using Hansen coefficients², and spatially, using spherical harmonics.

In Section 3.2, we employ these decompositions to compute the “passive deformation matrix” in terms of Love numbers, orbital eccentricity, mean motion ($n = \dot{M}$), and the spin angular velocities (ω and ω_α) of each body. The term “passive” refers to the fact that this deformation is computed while neglecting its influence on altering the orbital elements and the spin of each body.

2.3 Energy and angular momentum.

The energy function of a system of two rigid spherical bodies is

$$E_o := -\frac{Gmm_\alpha}{2a} + I_o \frac{\omega^2}{2} + I_{o\alpha} \frac{\omega_\alpha^2}{2} = -a_1 n^{2/3} + I_o \frac{\omega^2}{2} + I_{o\alpha} \frac{\omega_\alpha^2}{2}, \quad (2.5)$$

where: G is the gravitational constant, a is the semi-major axis, and

$$a_1 := \frac{mm_\alpha G^{2/3}}{(m + m_\alpha)^{1/3}}. \quad (2.6)$$

The angular momentum of a spherical body is $\ell_s = I_o \omega$ and the orbital angular momentum is

$$\ell = \frac{mm_\alpha}{m + m_\alpha} a^2 n \sqrt{1 - e^2} = a_1 n^{-1/3} \sqrt{1 - e^2}. \quad (2.7)$$

² If a is the semi-major axis, e is the eccentricity, and M is the mean anomaly, then

$$\left(\frac{r}{a}\right)^n e^{imf} = \sum_{k=-\infty}^{\infty} X_k^{n,m}(e) e^{ikM}, \quad (2.4)$$

where: n , m , and k are integers, and $X_k^{n,m}(e)$ is the Hansen coefficient.

The total angular momentum of a system of two spherical bodies is

$$\ell_T := \ell + \ell_s + \ell_{s\alpha}. \quad (2.8)$$

We will assume that $\ell > 0$ (or $n > 0$) and $\ell_T > 0$ for all time.

The energy and angular momentum of a system of two slightly deformable bodies, which are given in Section 3.1, are approximately given by the expressions of their spherical approximations.

The total angular momentum is constant, $\dot{\ell}_T = 0$, and within the Lagrangian formalism with dissipation function Ragazzo and Ruiz (2017) the time derivative of the energy is given by the sum of the dissipation functions of each body \mathcal{D} and \mathcal{D}_α .

In Section 3.3 we use the passive deformations to estimate the average dissipation of energy in each body. For the small body the result is:

$$\begin{aligned} \langle \mathcal{D} \rangle = & -\frac{3}{8} \left(\frac{m_\alpha}{m + m_\alpha} \right)^2 \frac{n^4 R^5}{G} \sum_{k=-\infty}^{\infty} \left\{ \frac{kn}{3} \left(X_k^{-3,0}(e) \right)^2 \operatorname{Im} k_2(kn) \right. \\ & \left. + (kn - 2\omega) \left(X_k^{-3,2}(e) \right)^2 \operatorname{Im} k_2(kn - 2\omega) \right\}. \end{aligned} \quad (2.9)$$

A similar expression holds for the α -body.

Since $\operatorname{Im} k_2(-\sigma) = -\operatorname{Im} k_2(\sigma)$ and $\operatorname{Im} k_2(\sigma) < 0$ for $\sigma > 0$, then $\langle \mathcal{D} \rangle \geq 0$. If $e = 0$, then $X_k^{-3,0}(0) = 0$ for $k \in \mathbb{Z}$ and $X_k^{-3,2}(0) = 0$ for $k \neq 2$. So $\langle \mathcal{D} \rangle = 0$ if and only if $e = 0$ and $n = \omega$.

The energy dissipated due to passive deformations must originate from the motion of the spherical bodies that induce these passive deformations. Consequently, we can infer

$$\begin{aligned} \dot{E}_o &= -\frac{2}{3} a_1 n^{-1/3} \dot{n} + I_o \omega \dot{\omega} + I_{o\alpha} \omega_\alpha \dot{\omega}_\alpha \\ &= -2\langle \mathcal{D} \rangle - 2\langle \mathcal{D}_\alpha \rangle. \end{aligned} \quad (2.10)$$

2.4 The average torque and the secular equation for the orbital elements

For the small body, the average torque due to passive deformations is:

$$\langle \mathbf{T} \rangle = -\frac{3}{2} \left(\frac{m_\alpha}{m + m_\alpha} \right)^2 \frac{n^4 R^5}{G} \left\{ \sum_{k=-\infty}^{\infty} \left(X_k^{-3,2} \right)^2 \operatorname{Im} k_2(kn - 2\omega) \right\}. \quad (2.11)$$

A similar expression holds for the α -body.

The secular equation for the orbital elements can be readily derived from equations (2.9), (2.10), (2.11), and their counterparts for the α -body:

$$\begin{aligned}\dot{\omega} &= \frac{1}{I_o} \langle \mathbf{T} \rangle, \\ \dot{\omega}_\alpha &= \frac{1}{I_{o\alpha}} \langle \mathbf{T}_\alpha \rangle, \\ \dot{n} &= \frac{3n^{1/3}}{2a_1} \left(2\langle \mathcal{D} \rangle + 2\langle \mathcal{D}_\alpha \rangle + \omega \langle \mathbf{T} \rangle + \omega_\alpha \langle \mathbf{T}_\alpha \rangle \right).\end{aligned}\tag{2.12}$$

The conservation of total angular momentum, combined with equations (2.7) and (2.8), implies that the eccentricity, which is featured on the right-hand side of equations (2.12), can be expressed in terms of the state variables ω, ω_α, n .

2.5 Time scales and a simplification when $m \ll m_\alpha$.

The despin rate is dependent on the imaginary parts of the Love numbers. The largest bodies in the solar system are fluid (e.g., the Sun, Jupiter, etc.) and have an imaginary part of the Love number that is significantly smaller than that of bodies with solid components. Therefore, it is reasonable to assume in the subsequent equations that either $\text{Im } k_2$ and $\text{Im } k_{2\alpha}$ are comparable or $\text{Im } k_2 \gg \text{Im } k_{2\alpha}$.

The ratio between the despin rates, assuming no spin-orbit resonances, is given by

$$\frac{\dot{\omega}}{\dot{\omega}_\alpha} \approx \frac{I_{o\alpha} m_\alpha^2 R^5}{I_o m^2 R_\alpha^5} \frac{\text{Im } k_2}{\text{Im } k_{2\alpha}} \approx \frac{\rho_\alpha m_\alpha^2}{\rho m^2} \frac{\text{Im } k_2}{\text{Im } k_{2\alpha}},\tag{2.13}$$

where ρ represents the density of the body. If $m_\alpha \gg m$, then $\dot{\omega} \gg \dot{\omega}_\alpha$, indicating that the despin rate of the larger body is significantly slower than that of the smaller body. In such a case, as a first approximation, we may assume $\omega_\alpha = \text{constant}$ and equations (2.12) become:

$$\begin{aligned}\dot{\omega} &= \frac{1}{I_o} \langle \mathbf{T} \rangle, \\ \dot{n} &= \frac{3n^{1/3}}{2a_1} \left(2\langle \mathcal{D} \rangle + 2\langle \mathcal{D}_\alpha \rangle + \omega \langle \mathbf{T} \rangle \right).\end{aligned}\tag{2.14}$$

For example, for the Sun-Mercury system, using $\text{Im } k_{2\alpha} \approx 3.5 \times 10^{-8}$ [Ogilvie \(2014\)](#) and $\text{Im } k_2 = 0.0051$ [Margot et al. \(2018\)](#), we obtain $\frac{\dot{\omega}}{\dot{\omega}_\alpha} \approx 2.8 \times 10^{17}$.

2.6 A simplification when the α body is fluid (almost inviscid).

The ratio of the energy dissipation rates in each body is given by

$$\frac{\langle \mathcal{D} \rangle}{\langle \mathcal{D}_\alpha \rangle} \approx \frac{m_\alpha^2 R^5}{m^2 R_\alpha^5} \frac{\text{Im } k_2}{\text{Im } k_{2\alpha}} \approx \frac{\rho_\alpha^2 R_\alpha}{\rho^2 R} \frac{\text{Im } k_2}{\text{Im } k_{2\alpha}}.\tag{2.15}$$

Equation (2.15), along with the equation for \dot{n} in (2.14), implies that depending on the imaginary parts of the Love numbers, the larger body may play a more significant role than the smaller body in altering the orbital elements³.

However, when the α body consists of a low viscosity fluid and the smaller body includes a solid part, then $\frac{\text{Im } k_2}{\text{Im } k_{2\alpha}} \gg 1$, and $\frac{\langle \mathcal{D} \rangle}{\langle \mathcal{D}_\alpha \rangle}$ may also be significantly greater than one. This scenario applies to the Sun-Mercury system, where $\frac{\langle \mathcal{D} \rangle}{\langle \mathcal{D}_\alpha \rangle} \approx 2.8 \times 10^6$. In such cases, $\langle \mathcal{D}_\alpha \rangle$ can be neglected in comparison to $\langle \mathcal{D} \rangle$ in the equation for \dot{n} in (2.14).

Therefore, for the Sun-Mercury system, we can employ the following approximation to equation (2.12):

$$\begin{aligned}\dot{\omega} &= \frac{1}{I_o} \langle T \rangle, \\ \dot{n} &= \frac{3n^{1/3}}{2a_1} \left(2\langle \mathcal{D} \rangle + \omega \langle T \rangle \right),\end{aligned}\tag{2.17}$$

where the state variables are (ω, n) . This type of equation commonly appears in the literature, as seen in references such as Correia et al. (2014), Gomes et al. (2019), and Correia and Valente (2022).

The angular momentum, which remains constant along the motion, becomes simpler:

$$\ell_T = a_1 n^{-1/3} \sqrt{1 - e^2} + I_o \omega.\tag{2.18}$$

Equations (2.17) are equivalent to those obtained in Correia and Valente (2022) in the planar case.

2.7 The dynamics when $\frac{I_o}{ma^2} \ll 1$.

In the remainder of this section, we consider the simplest case where equation (2.17) is applicable, with $m \ll m_\alpha$ and $\text{Im } k_{2\alpha} \ll \text{Im } k_2$.

The ratio

$$\frac{\dot{n}}{\dot{\omega}} = \frac{I_o n^{4/3}}{a_1} \frac{3\omega}{2n} \left\{ 1 + \frac{\frac{1}{2\omega} \left\{ \sum_{k=-\infty}^{\infty} \frac{k n}{3} \left(X_k^{-3,0}(e) \right)_{\text{Im } k_2(kn) + \dots}^2 \right\}}{\sum_{k=-\infty}^{\infty} \left(X_k^{-3,2} \right)_{\text{Im } k_2(kn - 2\omega)}^2} \right\}\tag{2.19}$$

³ For the Earth-Moon system, using the Love number $k_{2\alpha} = 0.2817 - 0.02324i$ for the Earth (Ragazzo and Ruiz, 2017, Table 3, semi-diurnal frequency), and $\text{Im } k_2 = 5.13 \times 10^{-4}$ for the Moon (orbital frequency) Fienga et al. (2019), we obtain

$$\frac{\langle \mathcal{D} \rangle}{\langle \mathcal{D}_\alpha \rangle} \approx \frac{m_\alpha^2 R^5 \text{Im } k_2}{m^2 R_\alpha^5 \text{Im } k_{2\alpha}} = 0.022.\tag{2.16}$$

This indicates that the Earth's influence on altering the orbital parameters is greater than that of the Moon.

includes the factor

$$\frac{I_o n^{4/3}}{a_1} = \frac{1}{m} \left(1 + \frac{m}{m_\alpha} \right) \frac{I_o}{a^2} \approx \frac{I_o}{m a^2}. \quad (2.20)$$

We assume

$$\frac{I_o n^{4/3}}{a_1} \approx \frac{I_o}{m a^2} \ll 1. \quad (2.21)$$

For the Sun-Mercury system,

$$\frac{I_o n^{4/3}}{a_1} = 6.2 \times 10^{-10}. \quad (2.22)$$

If $|\frac{\omega}{n}|$ is not far from one and (n, ω) is not on

$$\mathcal{C} := \left\{ (n, \omega) : \sum_{k=-\infty}^{\infty} \left(X_k^{-3,2}(e) \right)^2 \operatorname{Im} k_2(kn - 2\omega) = 0 \right\} \quad (\text{torque-free curve}), \quad (2.23)$$

then $\frac{\dot{\omega}}{n} \gg 1$. As a result, the spin-orbit dynamics is governed by a slow-fast system of equations, where n is the slow variable and ω is the fast variable. The typical dynamics is described in the caption of Figure 3.

Due to inequality (2.21), equation (2.18) can be simplified to

$$\frac{\ell_T}{n I_o} = \frac{a_1}{I_o n^{4/3}} \sqrt{1 - e^2} + \frac{\omega}{n} \approx \frac{a_1}{I_o n^{4/3}} \sqrt{1 - e^2}, \quad (2.24)$$

where we have used that $|\frac{\omega}{n}|$ is not far from one and e is not close to one. This leads to the approximation

$$e \approx \sqrt{1 - \left(\frac{\ell_T^3}{a_1^3} n \right)^{2/3}}. \quad (2.25)$$

The constant $\frac{\ell_T^3}{a_1^3}$ has the unit of time (for the Sun-Mercury system $\frac{\ell_T^3}{a_1^3} = 13.1224$ days⁴). We will use this constant to define the nondimensional mean motion ν and spin angular velocity w , which are used in several figures:

$$\nu := \frac{\ell_T^3}{a_1^3} n \quad w := \frac{\ell_T^3}{a_1^3} \omega. \quad (2.26)$$

⁴ $2\pi \frac{\ell_T^3}{a_1^3} = 82.45$ days is approximately the period of the longest possible synchronous, $\omega = n$, circular orbit of Mercury about the Sun.

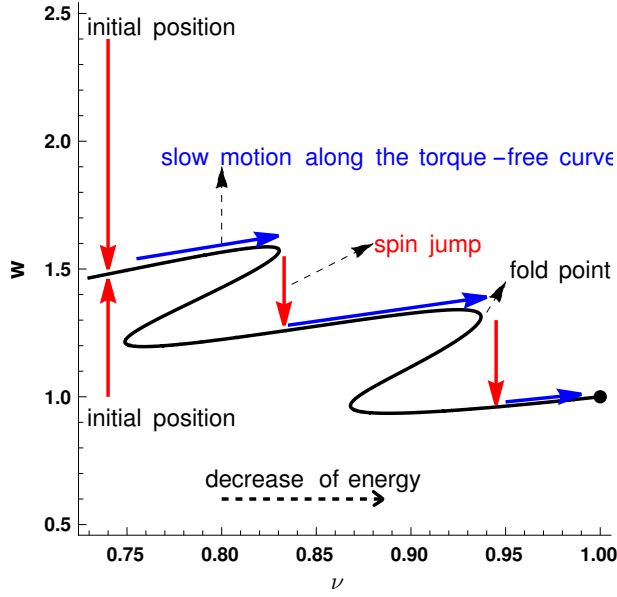


Fig. 3: Typical dynamics when $\frac{ma^2}{I_0} \gg 1$. We use the nondimensional mean motion $\nu = \frac{\ell_T^3}{a_1^3} n$ and the nondimensional spin angular velocity $w = \frac{\ell_T^3}{a_1^3} \omega$ in the plot, as seen in equation (2.26) and the previous paragraphs. The curve in black represents the torque-free curve \mathcal{C} : $\dot{w} < 0$ above \mathcal{C} , $\dot{w} > 0$ below \mathcal{C} , and $\dot{w} = 0$ on \mathcal{C} . An initial condition above \mathcal{C} converges rapidly to \mathcal{C} with a decreasing spin velocity, while an initial condition below \mathcal{C} converges rapidly to \mathcal{C} with an increasing spin velocity. Upon reaching \mathcal{C} , the solution gradually progresses along \mathcal{C} . The decrease in energy implies that ν increases along \mathcal{C} (with e decreasing). The motion along \mathcal{C} is sustainable up to a fold point. At this point, the decrease in energy forces the solution to depart from \mathcal{C} , resulting in a spin jump. The solution is then drawn towards another point on \mathcal{C} , representing a lower-order spin-orbit resonance. Eventually, the solution approaches the synchronous solution $(\nu, w) \approx (1, 1)$. For a general discussion on the flow close to \mathcal{C} , see Ragazzo and Ruiz (2024).

2.8 Characteristic times of terrestrial planets.

The imaginary part of the Love number of Mercury remains largely unknown, even at its orbital frequency Baland et al. (2017), Steinbrügge et al. (2018). The most well-studied terrestrial bodies in are the Earth and the Moon. It is reasonable to hypothesize that the rheology of Mercury could be similar, at least qualitatively, to those of the Earth and Moon.

Thirteen characteristic times and amplitudes of a five-layer interior model for the Moon [Matsuyama et al. \(2016\)](#) were computed in [Gevorgyan et al. \(2023\)](#). This research demonstrated that the complex Love number of the model can be effectively represented within the frequency range of interest by just three modes. These modes have nondimensional amplitudes h and characteristic times τ (in days) ([Gevorgyan et al. \(2023\)](#) Table 2 ⁵):

$$\begin{aligned}(h_1, \tau_1) &= (0.487, 12.2 \text{ d}), \\(h_2, \tau_2) &= (0.512, 18.3 \text{ d}), \\(h_3, \tau_3) &= (0.001, 8.3 \times 10^6 \text{ d}).\end{aligned}\tag{2.27}$$

A five-layer interior model for the Earth is presented in Table 2-1 in [Sabadini et al. \(2016\)](#). Nine relaxation times for this model, ranging from 2.6 to 2×10^5 centuries, are provided in ([Sabadini et al., 2016](#), p.64), but without corresponding amplitudes.

These examples demonstrate that terrestrial bodies, such as Mercury:

- May possess more than one relevant characteristic time,
- The relevant characteristic times can differ by orders of magnitude.

To investigate the importance of Mercury's rheology in the spin-orbit dynamics, we compare two different scenarios. In the first, Mercury is assumed to have a rheology with exactly one characteristic time τ . In the second scenario, Mercury is assumed to have a rheology with exactly two characteristic times τ_1 and τ_2 , such that $\tau_1 \ll \tau_2$ and $\tau_2 n_{mer} \gg 1$, where n_{mer} is the orbital mean motion.

2.9 Mercury's Love Number.

For Mercury, at the orbital frequency

$$n_{mer} = \frac{2\pi}{87.969 \text{ days}},\tag{2.28}$$

current estimates of the Love number fall within the range $0.53 < \text{Re } k_2 < 0.63$, with the preferred value being $k_2 = 0.569$ [Genova et al. \(2019\)](#), [Goossens et al. \(2022\)](#), and $0 < -\text{Im } k_2 < 0.025$ ([Baland et al., 2017](#), p. 152), ([Steinbrügge et al., 2018](#), p.2767 and 2769). We will assume $\text{Re } k_2 = 0.57$ and $-\text{Im } k_2 = 0.011$ as reference values (quality factor $Q \approx -\frac{\text{Re } k_2}{\text{Im } k_2} \approx 52$).

Mercury is not in hydrostatic equilibrium: the expected hydrostatic flattening is two orders of magnitude lower than the observed flattening. This discrepancy in hydrostaticity may be attributed to Mercury's despinning history [Matsuyama and Nimmo \(2009\)](#). According to [Ragazzo et al. \(2022\)](#) (Section 4.2), this suggests the presence of secular-elastic rigidity, represented by

⁵ The correspondence between the notation (s_j, r_j) in [Gevorgyan et al. \(2023\)](#) and that used here is: $s_j = -\tau_j^{-1}$, $r_j = h_j(k_o - k_\infty)$. The values of h_1, h_2, h_3 in (2.27) are normalized such that $h_1 + h_2 + h_3 = 1$

$\alpha_0 > 0$ in Figure 1, in conjunction with self-gravity, such that $k_o < k_f$, where k_f denotes the fluid Love number. Equation (2.2) implies that $k_f = 1.04$.

The choice of k_o within the range $[0.57, 1.04]$ is critical. One of the main results we present below – the significant enlargement of the basin of attraction of Mercury’s current state when transitioning from a rheology with one characteristic time to one with two characteristic times – does not hold if $k_o = k_f$. This highlights the importance of Mercury’s secular elastic rigidity in determining its current state. In our subsequent analysis, we will use $k_o = 0.8$ and $k_o = 0.7$.

2.10 Mercury with One Relaxation Time.

The generalized Voigt rheology (or standard solid rheology) with a single characteristic time is represented by a spring-dashpot model shown in Figure 1 with $n = 0$. The Love number is described by equation (2.1) with $n = 0$:

$$k_2(\sigma) = k_\infty + (k_o - k_\infty) \cdot \frac{1}{1 + i\tau\sigma}. \quad (2.29)$$

In Figure 4, we show the torque-free curve for the choice $k_o = 0.8$. Imposing $k_2(n_{mer}) = 0.57 - 0.011i$ we obtain $k_\infty = 0.5695$ and $\tau n_{mer} = 20.91$. Both the current state of Mercury and the stable synchronous equilibrium are also depicted. The current state of Mercury, as illustrated in Figure 4, suggests that Mercury must have been captured directly into the 3-2 spin-orbit resonance, without prior transitions through higher-order resonances.

In Figure 5, we show the torque-free curve for the choice $k_o = 0.7$. Imposing $k_2(n_{mer}) = 0.57 - 0.011i$ we obtain $k_\infty = 0.5691$ and $\tau n_{mer} = 11.89$. In this scenario, the current state of Mercury suggests that it could have been captured in a higher-order resonance before settling into the 3-2 spin-orbit resonance. The potential initial states of Mercury that lead to its current state, as indicated by the region hatched with vertical lines in Figure 5, encompass a much larger set than the corresponding region in Figure 4.

2.11 Mercury with Two Relaxation Times.

We assume a generalized Voigt rheology, equation (2.1) and Figure 1 with $n = 1$.

We choose $k_o = 0.8$ and fix the complex Love number at the orbital frequency as $k_2(n_{mer}) = 0.57 - 0.011i$. Equation (2.1) then implies

$$0.57 - 0.011i = k_\infty + (0.8 - k_\infty) \left(\frac{h_1}{1 + i\tau_1 n_{mer}} + \frac{h_2}{1 + i\tau_2 n_{mer}} \right) \quad (2.30)$$

with $h_1 > 0$, $h_2 > 0$, and $h_1 + h_2 = 1$. This results in a set of two scalar equations for the four unknowns: k_∞ , $0 < h_1 < 1$, $\tau_1 n_{mer}$, and $\tau_2 n_{mer}$.

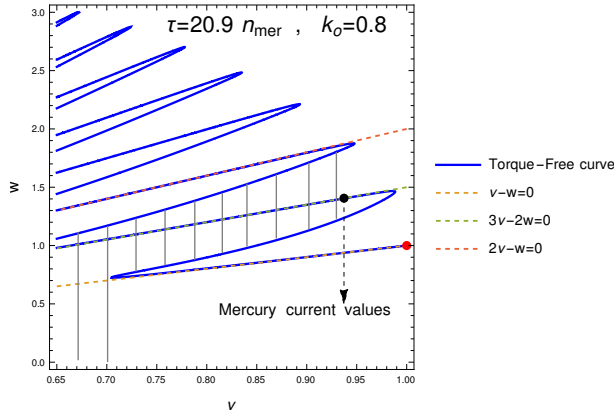


Fig. 4: Torque-free curve (blue) for Mercury with $k_o = 0.8$ and one relaxation time: $\tau n_{merc} = 20.91$. Three spin-orbit resonance lines (dashed) are shown. Mercury is currently on the $3n = 2\omega$ resonance line. The red point represents the synchronous equilibrium. The region hatched with vertical black lines represents potential initial positions of Mercury that could have led to its current state. The variables in the horizontal and vertical axes are: $\nu = \frac{\ell_T^3}{a_1^3} n$, $w = \frac{\ell_T^3}{a_1^3} \omega$, where $\frac{\ell_T^3}{a_1^3} = \frac{0.9373}{n_{mer}}$.

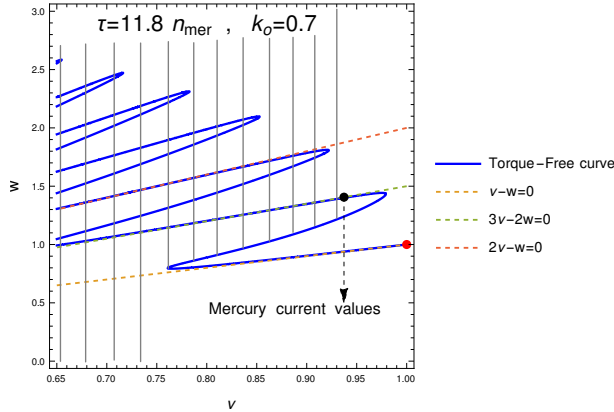


Fig. 5: Torque-free curve (blue) for Mercury with $k_o = 0.7$ and one relaxation time $\tau n_{mer} = 11.82$. The remainder of the notation is the same as that in Figure 4.

In Section 3.4, we demonstrate that equation (2.30) has solutions with arbitrarily large values of $\frac{T_2}{T_1}$. According to the models discussed in Section 2.8, the ratio between the largest and smallest relaxation times of both the Moon and Earth is of the order of 10^5 . Therefore, it would be logical to choose solu-

tions for equation (2.30) where $\frac{\tau_2}{\tau_1}$ is at least of order 10^5 . However, this choice presents numerical challenges in plotting the torque-free curve. Consequently, some plots presented below have a smaller ratio of $\frac{\tau_2}{\tau_1}$. As argued in Section 3.4, the conclusions drawn would remain valid for any larger value of $\frac{\tau_2}{\tau_1}$.

In Figure 6, we present the torque-free curve for the values: $\tau_1 n_{\text{mer}} = 0.48$, $\tau_2 n_{\text{mer}} = 1396$, $h_1 = 0.11$, $k_\infty = 0.5474$, which implies $k_2(n_{\text{mer}}) = 0.57 - 0.11 i$. In this scenario, the current state of Mercury suggests that it could have initially been captured in a higher-order resonance before transitioning to the 3-2 spin-orbit resonance. The potential initial states of Mercury that could lead to its current state, as indicated by the region hatched with vertical lines in Figure 6, encompass a much larger set than the corresponding region in Figure 4, which was derived using a rheology with a single relaxation time under the same constraints $k_2(n_{\text{mer}}) = 0.57 - 0.11 i$ and $k_o = 0.8$.

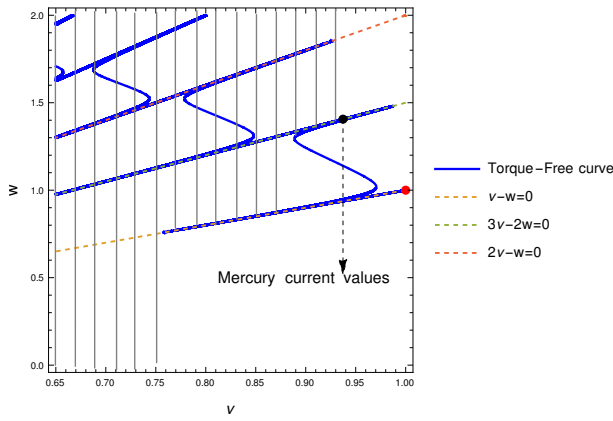


Fig. 6: Torque-free curve (blue) for Mercury with: $\tau_1 n_{\text{mer}} = 0.48$, $\tau_2 n_{\text{mer}} = 1396$, $h_1 = 0.11$, $h_2 = 0.89$, $k_\infty = 0.5474$. The remainder of the notation is the same as that in Figure 4.

In Figure 7, we illustrate the effect on the torque-free curve of increasing the ratio $\frac{\tau_2}{\tau_1}$ by a factor of 10. In both cases, the current state of Mercury suggests that it might have initially been captured in a higher-order resonance before transitioning to the 3-2 spin-orbit resonance. The conclusions regarding the set of initial conditions that lead to Mercury's current state, as established in Figure 6, are equally applicable to Figure 7.

The parameters used to generate Figure 6 do not accurately reflect the current state of Mercury, where $\omega = \frac{3}{2}n_{\text{mer}}$. According to equation (2.17) and with the parameters employed in Figure 6, the current rate of variation of Mercury's spin is $\frac{\dot{\omega}}{\omega} = \frac{1}{I_o \omega} \langle T \rangle = -2.5 \times 10^{-7} \text{ yr}^{-1}$. At this rate, over 10 million years, Mercury's spin would decrease to 10% of its current value. The same conclusion applies to the parameters used to generate Figure 7 and many other set of parameters that we tested. This may indicate that trapping into

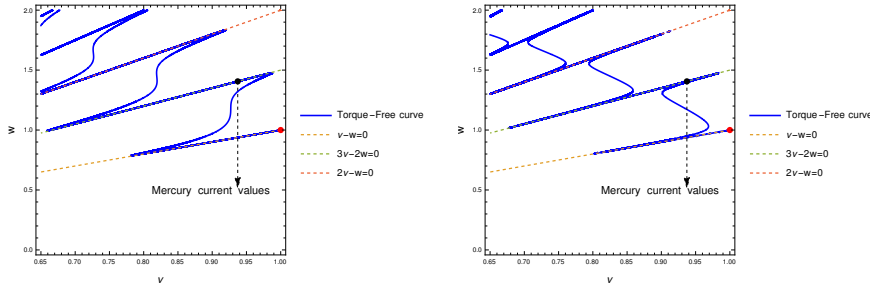


Fig. 7: Torque-free curve (blue) for Mercury. LEFT: $\tau_1 n_{\text{mer}} = 0.015, \tau_2 n_{\text{mer}} = 94, h_1 = 0.7126, k_{\infty} = 0$; and RIGHT: $\tau_1 n_{\text{mer}} = 0.019, \tau_2 n_{\text{mer}} = 940, h_1 = 0.7128, k_{\infty} = 0$.

the 3 : 2 spin-orbit resonance happened by means of a spin decrease and not the opposite.

The strong decay rate of the spin seems paradoxical in light of Mercury's current position in Figure 6, which appears to be on the torque-free curve. This paradox is elucidated in Figure 8 left, where we can observe that the gradient of the torque function at a point on the torque-free curve is very large. Consequently, the torque may still be nonnegligible even at points quite close to the torque-free curve. In Figure 8 right, we demonstrate that for $n = n_{\text{mer}}$, the value of $\frac{\omega}{n_{\text{mer}}}$ where the torque is zero is slightly below $\frac{3}{2}$, so Mercury is positioned above the torque-free curve.

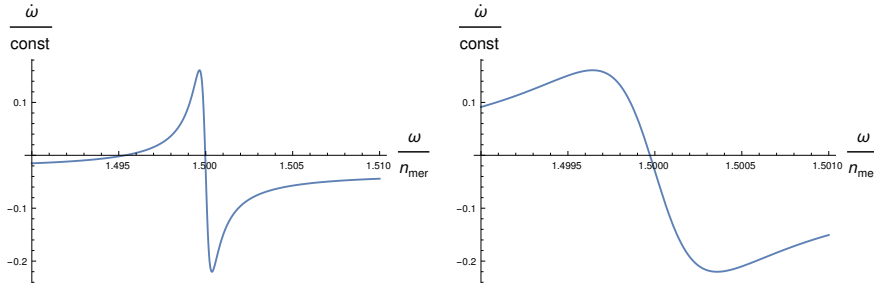


Fig. 8: Two graphs of $\dot{\omega} = \frac{\langle T \rangle}{I_{\circ}}$ divided by the constant $(k_{\circ} - k_{\infty}) \frac{3n_{\text{mer}}^4 R^5}{2G I_{\circ}} = 3.33 \times 10^{-19} \text{ s}^{-2}$ are presented as a function of $\frac{\omega}{n_{\text{mer}}}$. The parameters are those used in Figure 6. The graph on the left displays the two roots of $\dot{\omega}$, one of which appears to be at $\frac{\omega}{n_{\text{mer}}} = 1.5$. The graph on the right demonstrates that the root close to $\frac{\omega}{n_{\text{mer}}} = 1.5$ is actually slightly less than this value.

2.12 Conclusion

In this paper, we have obtained, by means of energy arguments, equations for the secular evolution of spin and orbit due to tidal effects. These equations were originally obtained by other authors, notably in [Correia and Valente \(2022\)](#). In the case of Mercury, which served as a model in our study on the dynamical effects of increasingly complex rheologies, the equations can be further simplified.

The main conclusion, which may be applicable to any binary system and not just Mercury-Sun, is that employing more complex and realistic rheologies is crucial in understanding spin-orbit evolution. This conclusion aligns with the findings in [Makarov \(2012\)](#) and [Noyelles et al. \(2014\)](#). According to the abstract of [Noyelles et al. \(2014\)](#): “As opposed to the commonly used constant time lag (CTL) and constant phase lag (CPL) models, the physics-based tidal model changes dramatically the statistics of the possible final spin states.” Here, the term “physics-based tidal model” refers to a model derived from a rheology with several relaxation times.

The past capture of Mercury into its current spin-orbit state has been the subject of several previous studies. In our paper, we have completely neglected several important effects that may have been significant, as pointed out in [Noyelles et al. \(2014\)](#): perturbations by other bodies in the Solar System that induce variations in Mercury’s eccentricity, the potential relevance of core-mantle-boundary friction at fluid-solid interfaces, the possibility of past impacts with other bodies, existence of a permanent deformation, and changes in the rheology over long time scales. Within this broader context, two aspects of Mercury’s rheology, which were crucial in our model, may still remain significant: 1) The elastic rigidity of Mercury at secular time scales, which must exist; otherwise, Mercury would be in hydrostatic equilibrium. 2) The presence of two or more relaxation times in Mercury’s rheology. Both these factors dramatically alter the probability of Mercury being captured in its current state. However, our quantitative results regarding the spin-orbit history of Mercury almost certainly do not align with what actually happened.

3 Mathematical Complements

In this section, we present several mathematical facts that explain and clarify many of the statements made in the previous section.

3.1 The fundamental equations

Let $\kappa := \{\mathbf{e}_1, \mathbf{e}_2, \mathbf{e}_3\}$ be an inertial orthonormal frame with origin at the centre of mass of the system. The orbit is contained in the plane $\{\mathbf{e}_1, \mathbf{e}_2\}$.

Let \mathbf{x} be the vector from the center of mass of the small body to the body α . The equation for the orbital motion is

$$\ddot{\mathbf{x}} = G(m_\alpha + m) \left\{ -\frac{\mathbf{x}}{|\mathbf{x}|^3} - \frac{15}{2} \frac{1}{|x|^7} \left(\left(\frac{I_{o\alpha}}{m_\alpha} \mathbf{b}_\alpha + \frac{I_o}{m} \mathbf{b} \right) \mathbf{x} \cdot \mathbf{x} \right) \mathbf{x} + 3 \frac{1}{|\mathbf{x}|^5} \left(\frac{I_{o\alpha}}{m_\alpha} \mathbf{b}_\alpha + \frac{I_o}{m} \mathbf{b} \right) \mathbf{x} \right\}, \quad (3.31)$$

where the deformation matrix of the small body \mathbf{b} , defined in equation (2.3), is given by

$$\mathbf{b} = \begin{pmatrix} b_{11} & b_{12} & 0 \\ b_{12} & b_{22} & 0 \\ 0 & 0 & b_{33} \end{pmatrix}, \quad \text{with } b_{33} = -b_{11} - b_{22}. \quad (3.32)$$

For a rigid body, there exists a frame, namely the body frame, in which the body remains at rest. Specifically, the angular momentum of the body with respect to the body frame is null. In the case of a deformable body, a frame still exists where the body's angular momentum is null: this is known as the Tisserand frame. Let $\mathbf{K} := \{\mathbf{e}_{T1}, \mathbf{e}_{T2}, \mathbf{e}_{T3}\}$ denote an orthonormal Tisserand frame for the small body. The orientation of \mathbf{K} with respect to the inertial frame $\kappa = \{\mathbf{e}_1, \mathbf{e}_2, \mathbf{e}_3\}$ is described by $\mathbf{R} : \mathbf{K} \rightarrow \kappa$. We assume that the angular velocity of the small body, $\boldsymbol{\omega}$, is perpendicular to the orbital plane, which implies :

$$\mathbf{R}(\phi) = \begin{pmatrix} \cos \phi & -\sin \phi & 0 \\ \sin \phi & \cos \phi & 0 \\ 0 & 0 & 1 \end{pmatrix}, \quad (3.33)$$

with $\boldsymbol{\omega} = \omega \mathbf{e}_3 = \dot{\phi} \mathbf{e}_3$.

The angular momentum of the small body is denoted by $\ell_s = \ell_s \mathbf{e}_3$, with the index s representing spin, and is given by:

$$\ell_s = \omega I_o (1 - b_{33}). \quad (3.34)$$

In the context of the quadrupolar approximation, Euler's equation for the variation of ℓ_s is:

$$\dot{\ell}_s = -\frac{3G I_o m_\alpha}{\|\mathbf{x}\|^5} \left\{ x_1 x_2 (b_{22} - b_{11}) + b_{12} (x_1^2 - x_2^2) \right\}. \quad (3.35)$$

A similar equation holds for the large body.

It is imperative to note that, unlike the case of a rigid body, the deformation matrix is not constant in the Tisserand frame \mathbf{K} .

To complete the set of equations (3.31) and (3.35), we require additional equations for the deformation matrices. These equations were derived within the Lagrangian formalism and utilizing what was termed the ‘‘Association Principle’’, as detailed in Ragazzo and Ruiz (2015), Ragazzo and Ruiz (2017).

In the Tisserand frame \mathbf{K} of the small body, the deformation matrix and the position vector are denoted by capital letters as follows:

$$\mathbf{B} = \mathbf{R}(\phi)\mathbf{b}\mathbf{R}^{-1}(\phi) \quad \mathbf{X} = \mathbf{R}^{-1}(\phi)\mathbf{x}. \quad (3.36)$$

The equations for the deformation variables of the smaller body for the generalised Voigt model in Figure 1 are (Ragazzo et al., 2022, Eq. (3.15))

$$\begin{aligned} (\gamma + \alpha_0)\mathbf{B} + \mathbf{\Lambda} &= \mathbf{F} \\ \frac{1}{\alpha}\dot{\mathbf{\Lambda}} + \frac{1}{\eta}\mathbf{\Lambda} &= \dot{\mathbf{B}} \\ \eta_j\dot{\mathbf{B}}_j + \alpha_j\mathbf{B}_j &= \mathbf{\Lambda}, \quad j = 1, \dots, n \\ \mathbf{B} &= \tilde{\mathbf{B}} + \mathbf{B}_1 + \mathbf{B}_2 + \dots + \mathbf{B}_n, \end{aligned} \quad (3.37)$$

where:

- γ , with dimensions of $1/\text{time}^2$, is a parameter representing the self-gravity rigidity of the body; a larger γ indicates a stronger gravitational force holding the body together. In Figure 1 γ would be a spring in parallel to the spring-dashpot system representing the rheology.
- $\alpha_0, \alpha, \alpha_1, \dots$ also with dimensions of $1/\text{time}^2$, are elastic rigidity coefficients; α increases with the stiffness.
- η, η_1, \dots , dimensions of $1/\text{time}$, are viscosity parameters; a body with a larger η is harder to deform at a given rate compared to a body with a smaller η .
- $\tilde{\mathbf{B}}, \mathbf{B}_1, \dots$, are nondimensional traceless matrices that represent internal variables of the rheology;
- $\mathbf{\Lambda}$, with dimensions $1/\text{time}^2$, is a traceless force matrix that represents the stress upon the rheology part ($\mathbf{F} - \mathbf{\Lambda}$ is the stress supported by self-gravity).
- \mathbf{F} , with dimensions $1/\text{time}^2$, is the force matrix in the Tisserand frame \mathbf{K} :

$$\begin{aligned} \mathbf{F} &:= \mathbf{C} + \mathbf{S} && \text{Deformation force} \\ \mathbf{C} &:= \frac{\omega^2}{3} \begin{pmatrix} 1 & 0 & 0 \\ 0 & 1 & 0 \\ 0 & 0 & -2 \end{pmatrix} && \text{Centrifugal force} \\ \mathbf{S} &:= \frac{3Gm_\alpha}{|\mathbf{X}|^5} \left(\mathbf{X}\mathbf{X}^T - \frac{|\mathbf{X}|^2}{3}\mathbf{1} \right) && \text{Tidal force} \end{aligned} \quad (3.38)$$

where \mathbf{X} is understood as a column vector, \mathbf{X}^T is the transpose of \mathbf{X} (a row vector), and $\mathbf{X}\mathbf{X}^T$ is the usual product of a $n \times 1$ by $1 \times n$ matrix, which gives an $n \times n$ matrix with entries $(\mathbf{X}\mathbf{X}^T)_{ij} = X_i X_j$. The norm of a matrix is defined as $\|\mathbf{B}\|^2 = \frac{1}{2} \text{Tr}(\mathbf{B}^T \mathbf{B})$.

Conservation of angular momentum. The orbital angular momentum is given by

$$\ell \mathbf{e}_3 = \boldsymbol{\ell} = \frac{m_\alpha m}{m_\alpha + m} \mathbf{x} \times \dot{\mathbf{x}}. \quad (3.39)$$

From equations (3.31) and (3.35) we obtain

$$\dot{\boldsymbol{\ell}} = 3 \frac{m_\alpha m}{|\mathbf{x}|^5} \mathbf{x} \times \left(\frac{\mathbf{I}_{o\alpha}}{m_\alpha} \mathbf{B}_\alpha + \frac{\mathbf{I}_o}{m} \mathbf{B} \right) \mathbf{x} = -\dot{\boldsymbol{\ell}}_{s\alpha} - \dot{\boldsymbol{\ell}}_s, \quad (3.40)$$

that shows the conservation of total angular momentum

$$\boldsymbol{\ell}_T := \boldsymbol{\ell} + \boldsymbol{\ell}_{s\alpha} + \boldsymbol{\ell}_s. \quad (3.41)$$

Energy. The total energy of the system is

$$E = E_{kcm} + E_{krot} + E_{def} + E_{gr} \quad (3.42)$$

where:

$$E_{kcm} = \frac{m_\alpha m}{m_\alpha + m} \frac{|\dot{\mathbf{x}}|^2}{2} \quad (3.43)$$

is the kinetic energy of the orbital motion;

$$E_{krot} = \frac{\boldsymbol{\omega}_\alpha \cdot \mathbf{I}_\alpha \boldsymbol{\omega}_\alpha}{2} + \frac{\boldsymbol{\omega} \cdot \mathbf{I} \boldsymbol{\omega}}{2} \quad (3.44)$$

is the kinetic energy of rotation;

$$E_{def} = \frac{\mathbf{I}_o}{2} \left((\gamma + \alpha_0) \|\mathbf{B}\|^2 + \frac{\|\boldsymbol{\Lambda}\|^2}{\alpha} + \sum_{j=1}^n \alpha_j \|\mathbf{B}_j\|^2 \right) + \text{Large body term} \quad (3.45)$$

is the elastic energy of deformation of the generalised Voigt model in Figure 1; and

$$E_{gr} = -\frac{Gm_\alpha m}{|\mathbf{x}|} - \frac{3G}{2} \frac{1}{|\mathbf{x}|^5} \{m\mathbf{I}_{o\alpha}(\mathbf{x} \cdot \mathbf{B}_\alpha \mathbf{x}) + m_\alpha \mathbf{I}_o(\mathbf{x} \cdot \mathbf{B} \mathbf{x})\} \quad (3.46)$$

is the potential energy due to gravitational interactions.

Dissipation of energy. For the generalised Voigt model in Figure 1, the dissipation function of the small body is:

$$\mathcal{D} = \frac{\mathbf{I}_o}{2} \left(\frac{\|\boldsymbol{\Lambda}\|^2}{\eta} + \sum_{j=1}^n \eta_j \|\dot{\mathbf{B}}_j\|^2 \right) \quad (3.47)$$

A similar expression \mathcal{D}_α holds for the large body. The Lagrangian formalism with dissipation function [Ragazzo and Ruiz \(2015\)](#), [Ragazzo and Ruiz \(2017\)](#) implies that the total energy decreases along the motion:

$$\dot{E} = -(2\mathcal{D} + 2\mathcal{D}_\alpha) \leq 0. \quad (3.48)$$

Moreover, $2\mathcal{D}_\alpha$ and $2\mathcal{D}$ are the powers dissipated within the large and small bodies, respectively.

The secular equations (2.12) are approximations to the fundamental equations presented in this Section.

3.2 Computation of the Passive Deformation Matrix.

Passive deformation refers to the tides caused by an orbiting point mass on an extended body, while the influence of the gravitational field, resulting from the deformation on the orbit, is neglected. The equations that describe these passive deformations are obtained setting $\mathbf{B} = \mathbf{B}_\alpha = 0$ in equations (3.31) and (3.35) while preserving equation (3.37):

$$\begin{aligned} \ddot{\mathbf{x}} &= -G(m_\alpha + m) \frac{\mathbf{x}}{|\mathbf{x}|^3}, \quad \dot{\omega} = 0, \quad \dot{\omega}_\alpha = 0 \\ (\gamma + \alpha_0)\mathbf{B} + \mathbf{\Lambda} &= \mathbf{F} \\ \frac{1}{\alpha}\dot{\mathbf{\Lambda}} + \frac{1}{\eta}\mathbf{\Lambda} &= \dot{\mathbf{B}} \\ \eta_j\dot{\mathbf{B}}_j + \alpha_j\mathbf{B}_j &= \mathbf{\Lambda}, \quad j = 1, \dots, n \\ \mathbf{B}_T &= \dot{\mathbf{B}} + \mathbf{B}_1 + \mathbf{B}_2 + \dots + \mathbf{B}_n. \end{aligned} \quad (3.49)$$

Plus deformation equations for the large body

In this scenario ω and ω_α remain constant and \mathbf{x} follows a Keplerian ellipse.

In order to write the \mathbf{F} in a convenient way, we define the matrices (Ragazzo and Ruiz, 2017, Eq. (41))

$$\mathbf{Y}_0 := \frac{1}{\sqrt{3}} \begin{pmatrix} 1 & 0 & 0 \\ 0 & 1 & 0 \\ 0 & 0 & -2 \end{pmatrix}, \quad \mathbf{Y}_1 := \frac{1}{\sqrt{2}} \begin{pmatrix} 0 & 0 & 1 \\ 0 & 0 & -i \\ 1 & -i & 0 \end{pmatrix}, \quad \mathbf{Y}_2 := \frac{1}{\sqrt{2}} \begin{pmatrix} 1 & -i & 0 \\ -i & -1 & 0 \\ 0 & 0 & 0 \end{pmatrix}, \quad (3.50)$$

$\mathbf{Y}_{-1} = \overline{\mathbf{Y}}_1$, and $\mathbf{Y}_{-2} = \overline{\mathbf{Y}}_2$, where the overline represents complex conjugation.

Any symmetric matrix can be written as a linear combination of the six matrices $\{\mathbf{1}, \mathbf{Y}_{-2}, \mathbf{Y}_{-1}, \mathbf{Y}_0, \mathbf{Y}_1, \mathbf{Y}_2\}$. This basis is orthonormal with respect to the Hermitean inner product $\mathbf{A} \cdot \mathbf{B} = \frac{1}{2} \text{Tr}(\overline{\mathbf{A}}^T \mathbf{B}) = \frac{1}{2} \sum_{ij} \overline{A}_{ij} B_{ij}$.

Traceless matrices that are invariant under rotation with respect to the \mathbf{e}_3 -axis can be written as linear combinations of $\{\mathbf{Y}_{-2}, \mathbf{Y}_0, \mathbf{Y}_2\}$. These matrices have a simple transformation rule with respect to rotations about the axis \mathbf{e}_3 , namely

$$\mathbf{R}(\theta)\mathbf{Y}_j\mathbf{R}^{-1}(\theta) = e^{ij\theta} \mathbf{Y}_j, \quad j = -2, 0, 2. \quad (3.51)$$

An elliptic orbit in the body frame is given by

$$\begin{aligned} \mathbf{X} &= \mathbf{R}^{-1}(\phi)\mathbf{x} = r\mathbf{R}(f + \varpi - \phi)\mathbf{e}_1 \\ &= r(\cos(f + \varpi - \phi)\mathbf{e}_1 + \sin(f + \varpi - \phi)\mathbf{e}_2), \end{aligned} \quad (3.52)$$

where f is the mean anomaly, ϖ is the argument of the periapsis.

The associated tidal-force matrix, equation (3.38), can be written as

$$\begin{aligned} \mathbf{S} &= \frac{3Gm_\alpha}{r^3} \mathbf{R}_3(f + \varpi - \phi) \left\{ \mathbf{e}_1 \mathbf{e}_1^T - \frac{1}{3} \mathbf{1} \right\} \mathbf{R}_3^{-1}(f + \varpi - \phi) \\ &= \frac{3Gm_\alpha}{2r^3} \left\{ e^{-2i(f + \varpi - \phi)} \frac{\mathbf{Y}_{-2}}{\sqrt{2}} + \frac{\mathbf{Y}_0}{\sqrt{3}} + e^{2i(f + \varpi - \phi)} \frac{\mathbf{Y}_2}{\sqrt{2}} \right\}. \end{aligned} \quad (3.53)$$

In equation (3.53), the variables r , f , and $\phi = \omega t$ are dependent on t .

Equations (3.53) and (2.4) gives a harmonic decomposition of the tidal force as follows:

$$\mathbf{S} = \frac{3Gm_\alpha}{2a^3} \sum_{l=-2}^2 \sum_{k=-\infty}^{\infty} e^{i\{t(kn-l\omega)+l\varpi\}} \mathbf{Y}_l U_{kl}, \quad (3.54)$$

where $U_{k,-1} = U_{k,1} = 0$ and

$$U_{k,-2} = \frac{X_k^{-3,-2}}{\sqrt{2}}, \quad U_{k0} = \frac{X_k^{-3,0}}{\sqrt{3}}, \quad U_{k2} = \frac{X_k^{-3,2}}{\sqrt{2}}. \quad (3.55)$$

The symmetry property $X_{-k}^{n,-m} = X_k^{n,m}$ implies $U_{kj} = U_{-k,-j}$.

The centrifugal force in equation (3.38) can be represented as

$$\mathbf{C} = \frac{\omega^2}{\sqrt{3}} \mathbf{Y}_0. \quad (3.56)$$

To obtain the almost periodic solution of the deformation equation solving for each Fourier mode separately suffices.

To simplify the notation we consider a simple harmonic force term of the form

$$\mathbf{F}(t) = \mathbf{F}' e^{i\sigma t}$$

where \mathbf{F}' is a complex amplitude matrix, and $\sigma \in \mathbb{R}$ is the constant forcing frequency.

If we do the substitutions

$$\mathbf{B} \rightarrow \mathbf{B}' e^{i\sigma t}, \quad \mathbf{B}_j \rightarrow \mathbf{B}'_j e^{i\sigma t}, \quad \mathbf{\Lambda} \rightarrow \mathbf{\Lambda}' e^{i\sigma t},$$

where \mathbf{B}' , \mathbf{B}'_j and $\mathbf{\Lambda}'_j$ are understood as constant complex-amplitude matrices, into equation (3.37), then we obtain after some simplifications

$$\left\{ \gamma + \alpha_0 + \left(\frac{1}{\alpha} + \frac{1}{\eta i \sigma} + \sum_{j=1}^n \frac{1}{\alpha_j + i\sigma \eta_j} \right)^{-1} \right\} \mathbf{B}' = \mathbf{F}'. \quad (3.57)$$

The term $\frac{1}{\alpha} + \frac{1}{\eta i \sigma} + \sum_{j=1}^n \frac{1}{\alpha_j + i\sigma \eta_j}$ is the complex rigidity $J(\sigma)$ of the generalised Voigt model when $\alpha_0 = 0$ (Ragazzo et al., 2022, equation 4.23).

The complex Love number at frequency σ can be written as (Correia et al., 2018, Section 4):

$$k_2(\sigma) = \frac{3\mathbf{I}_0 G}{R^5} \frac{1}{\gamma + \alpha_0 + J^{-1}(\sigma)}. \quad (3.58)$$

Note: $k_2(-\sigma) = \bar{k}_2(\sigma)$. Therefore, equation (3.57) can be written as

$$\mathbf{B}' = \frac{R^5}{3\mathbf{I}_0 G} k_2(\sigma) \mathbf{F}'. \quad (3.59)$$

Applying equation (3.59) to each Fourier coefficient of $\mathbf{F} = \mathbf{S} + \mathbf{C}$, where \mathbf{S} and \mathbf{C} are defined in equations (3.54) and (3.56) respectively, we obtain the passive-deformation matrix

$$\mathbf{B}(t) = k_o \zeta_c \frac{\mathbf{Y}_0}{3\sqrt{3}} + \zeta_r \sum_{l=-2}^2 \sum_{k=-\infty}^{\infty} e^{i\{t(kn-l\omega)+l\varpi\}} k_2(kn-l\omega) \mathbf{Y}_l U_{kl}, \quad (3.60)$$

where $k_o = k_2(0)$ is the secular Love number and

$$\zeta_c := \frac{R^5 \omega^2}{G I_o} \quad \text{and} \quad \zeta_r := \frac{m_\alpha R^5}{2 I_o a^3}. \quad (3.61)$$

3.3 The Average Dissipation of Energy and Average Torque.

The energy dissipated in the smaller body is $-2\mathcal{D}$, where \mathcal{D} is the dissipation function as given in equation (3.47). The average dissipation function over the orbital motion is approximately given by

$$\langle \mathcal{D} \rangle := \lim_{t \rightarrow \infty} \int_0^T \mathcal{D} dt = \frac{I_o}{2} \lim_{t \rightarrow \infty} \int_0^T \left(\frac{\|\mathbf{\Lambda}\|^2}{\eta} + \sum_{j=1}^n \eta_j \|\dot{\mathbf{B}}_j\|^2 \right) dt, \quad (3.62)$$

where $(\mathbf{B}, \mathbf{\Lambda}, \dots)$ are the components of the solution to equation (3.37) under the passive deformation hypothesis.

From equation (3.37) we obtain:

$$\begin{aligned} (\gamma + \alpha_0) \langle \dot{\mathbf{B}} \cdot \mathbf{B} \rangle + \langle \dot{\mathbf{B}} \cdot \mathbf{\Lambda} \rangle &= \langle \dot{\mathbf{B}} \cdot \mathbf{C} \rangle + \langle \dot{\mathbf{B}} \cdot \mathbf{S} \rangle \\ \frac{1}{\alpha} \langle \mathbf{\Lambda} \cdot \dot{\mathbf{\Lambda}} \rangle + \frac{1}{\eta} \|\mathbf{\Lambda}\|^2 &= \langle \mathbf{\Lambda} \cdot \dot{\mathbf{B}} \rangle \\ \eta_j \|\dot{\mathbf{B}}_j\|^2 + \alpha_j \langle \dot{\mathbf{B}}_j \cdot \mathbf{B}_j \rangle &= \langle \dot{\mathbf{B}}_j \cdot \mathbf{\Lambda} \rangle, \quad j = 1, \dots, n \\ \langle \dot{\mathbf{B}} \cdot \mathbf{\Lambda} \rangle &= \langle \dot{\mathbf{B}} \cdot \mathbf{\Lambda} \rangle + \langle \dot{\mathbf{B}}_1 \cdot \mathbf{\Lambda} \rangle + \langle \dot{\mathbf{B}}_2 \cdot \mathbf{\Lambda} \rangle + \dots + \langle \dot{\mathbf{B}}_n \cdot \mathbf{\Lambda} \rangle, \end{aligned} \quad (3.63)$$

where we used that the centrifugal force \mathbf{C} , equation (3.56), is constant. These equations imply

$$\langle \mathcal{D} \rangle = \frac{I_o}{2} \langle \dot{\mathbf{B}} \cdot \mathbf{S} \rangle, \quad (3.64)$$

where \mathbf{S} and \mathbf{B} are given in equations (3.54) and (3.60), respectively.

In the computation of the averaging $\langle \dot{\mathbf{B}} \cdot \mathbf{S} \rangle$ the following identities are useful: $\mathbf{Y}_l \cdot \mathbf{Y}_{-m} = \delta_{lm}$, $U_{kl} = U_{-k, -l}$, and $k_2(-\sigma) = \bar{k}_2(\sigma)$. After some computations we obtain equation (2.9).

The total energy, as given in equation (3.42), includes terms that depend on the deformation matrices. If we set $\mathbf{B} = \mathbf{B}_\alpha = 0$ in this equation and assume that the orbit is Keplerian and the spins are constant, then we obtain the energy function E_o , as presented in equation (2.5), for a system of two rigid spherical bodies. It is a natural assumption that the energy dissipated

in the two bodies is subtracted from E_o . This assumption leads to equation (2.10).

The average torque is computed as the average of the right-hand side of equation (3.35),

$$\langle T \rangle := \lim_{t \rightarrow \infty} \int_0^t -\frac{3GI_o m_\alpha}{\|\mathbf{x}\|^5} \left\{ x_1 x_2 (b_{22} - b_{11}) + b_{12} (x_1^2 - x_2^2) \right\} dt, \quad (3.65)$$

where \mathbf{B} represents the passive deformation matrix and \mathbf{x} determines Keplerian ellipses. Standard computations lead to equation (2.11).

Equations (2.10) and (2.11) imply equations (2.12).

3.4 Solutions to Equation (2.30) for $\tau_2 n_{\text{mer}} \gg 1$ and the Torque-Free Curve for $\tau_2/\tau_1 \gg 1$

If $\tau_2 n_{\text{mer}} \gg 1$, then equation (2.30) can be approximately written as

$$\frac{0.57 - k_\infty}{0.8 - k_\infty} - \frac{0.011}{0.8 - k_\infty} i = \frac{h_1}{1 + i\tau_1 n_{\text{mer}}} - i \frac{1 - h_1}{\tau_2 n_{\text{mer}}}. \quad (3.66)$$

The left-hand side defines a curve in the complex plane, parameterized by $k_\infty \in [0, 0.57]$. As $\tau_2 \rightarrow \infty$, the right-hand side converges to $\frac{h_1}{1 + i\tau_1 n_{\text{mer}}}$, and for a given $h_1 \in (0, 1)$, it defines a curve in the complex plane, parameterized by $\tau_1 \in (0, \infty)$. This curve is a semi-circle below the real axis, with a radius of $\frac{h_1}{2}$ and centered at $(\frac{h_1}{2}, 0)$. In the limit as $\tau_2 \rightarrow \infty$, for a given h_1 , the solution to equation (3.66) is represented by a pair (k_∞, τ_1) , corresponding to the intersection of these two curves, as illustrated in Figure 9.

In the following, we graphically demonstrate how to obtain a solution to equation (2.30) for $\tau_2 n_{\text{mer}} \gg 1$, using the solution marked with a ball in Figure 9.

For the fixed value of $h_1 = 0.11$, we choose $\tau_1 n_{\text{mer}}$ to be slightly smaller than 0.492353, which corresponds to the solution marked in Figure 9, say $\tau_1 n_{\text{mer}} = 0.48$. The curve parameterized by $\tau_1 \in [0, 0.48/n_{\text{mer}}]$ (blue) will terminate slightly above the curve parameterized by k_∞ (red). Substituting $h_1 = 0.11$ and $\tau_1 n_{\text{mer}} = 0.48$ into equation (3.66), we obtain

$$\frac{0.57 - k_\infty}{0.8 - k_\infty} - \frac{0.011}{0.8 - k_\infty} i = \frac{0.11}{1 + i0.48} - i \frac{0.89}{\tau_2 n_{\text{mer}}}. \quad (3.67)$$

Now, the right-hand side of equation (3.67) defines a vertical segment in the complex plane starting at $\frac{0.11}{1 + i0.48}$ for $\tau_2 = +\infty$, and decreasing to $-\infty i$ as $\tau_2 \rightarrow 0$. This curve clearly intersects the curve parameterized by k_∞ , as depicted in Figure 10. As $\tau_1 n_{\text{mer}}$ approaches 0.492353 from below, the value of $\tau_2 n_{\text{mer}}$ increases towards $+\infty$.

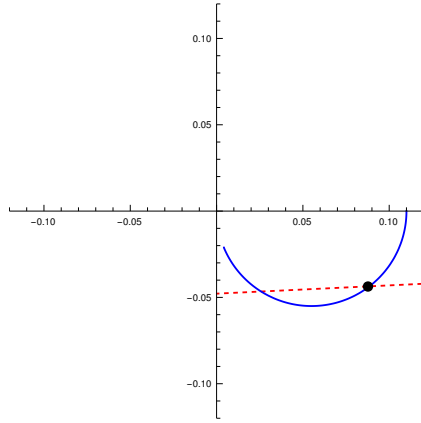


Fig. 9: Graphical solution to equation (3.66) in the limit as $\tau_2 \rightarrow \infty$ for $h_1 = 0.11$. The dashed-red curve is parameterized by k_∞ , while the blue curve is parameterized by τ_1 . The intersections of these curves represent the solutions $(k_\infty, \tau_1 n_{mer})$, specifically: $(0.547658, 0.492353)$, which is marked by a ball, and $(0.563915, 1.80765)$.

An application of the implicit function theorem to equation (3.66) around the solution $(k_\infty, \tau_1 n_{mer}, (\tau_2 n_{mer})^{-1}) = (0.547658, 0.492353, 0)$ yields the following formula:

$$k_\infty = 0.547658 - \frac{0.341496}{\tau_2 n_{mer}}, \quad \tau_1 n_{mer} = 0.492353 - \frac{17.5779}{\tau_2 n_{mer}}. \quad (3.68)$$

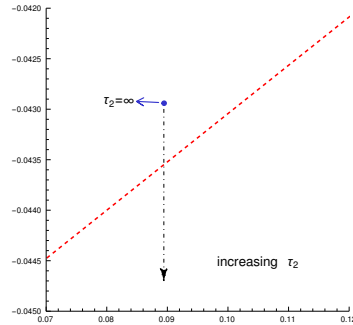


Fig. 10: Graphical solution to equation (3.67) for $\tau_2 n_{mer} \gg 1$ and $h_1 = 0.11$. The dashed-dotted-black line is parameterized by τ_2 .

As previously mentioned, plotting the torque-free curve is numerically challenging when $\tau_1 \ll \tau_2$. In this limit, it is possible to approximate the torque-free curve near a given resonance line, $k_* n - 2\omega = 0$, as demonstrated in the following paragraphs.

First, we substitute the variable ω with ϵ using the equation $k_*n - 2\omega = -2\epsilon$. The analysis will be confined to a neighborhood of the resonance line, namely

$$|\epsilon|\tau_2 < 1.$$

We write equation (2.23), for the torque-free curve, using the new variable

$$0 = -\frac{1}{k_o - k_\infty} \sum_{k=-\infty}^{\infty} \left(X_k^{-3,2}(e) \right)^2 \text{Im } k_2((k - k_*)n - 2\epsilon) = \sum_{k=-\infty}^{\infty} \left(X_k^{-3,2}(e) \right)^2 \left(\frac{h_1 \tau_1 ((k - k_*)n - 2\epsilon)}{1 + \tau_1^2 ((k - k_*)n - 2\epsilon)^2} + \frac{(1 - h_1) \tau_2 ((k - k_*)n - 2\epsilon)}{1 + \tau_2^2 ((k - k_*)n - 2\epsilon)^2} \right).$$

For $k \neq k_*$, where $|\pm n - 2\epsilon| > \text{constant} > 0$, and $\tau_2 \gg 1$,

$$\left| \frac{\tau_2 ((k - k_*)n - 2\epsilon)}{1 + \tau_2^2 ((k - k_*)n - 2\epsilon)^2} \right| < \left| \frac{1}{\tau_2 ((k - k_*)n - 2\epsilon)} \right| \approx 0,$$

and the equation for the torque-free curve can be approximately written as

$$\sum_{k=-\infty}^{\infty} \frac{\left(X_k^{-3,2}(e) \right)^2}{\left(X_{k_*}^{-3,2}(e) \right)^2} \frac{\tau_1 ((k - k_*)n - 2\epsilon)}{1 + \tau_1^2 ((k - k_*)n - 2\epsilon)^2} = \frac{1 - h_1}{h_1} \frac{2\tau_2 \epsilon}{1 + (2\tau_2 \epsilon)^2},$$

where, according to approximation (2.25), $e = \sqrt{1 - \left(\frac{\ell_T^3}{a_1^3} n\right)^{2/3}}$. It is convenient to rewrite this equation using the variables $\nu := \frac{\ell_T^3}{a_1^3} n$, $w := \frac{\ell_T^3}{a_1^3} \omega$, $T_1 := \frac{a_1^3}{\ell_T^3} \tau_1$, and $x = 2\epsilon\tau_2$:

$$\sum_{k=-\infty}^{\infty} \frac{\left(X_k^{-3,2}(e) \right)^2}{\left(X_{k_*}^{-3,2}(e) \right)^2} \frac{((k - k_*)T_1\nu - \frac{T_1}{\tau_2}x)}{1 + \left((k - k_*)T_1\nu - \frac{T_1}{\tau_2}x \right)^2} = \frac{1 - h_1}{h_1} \frac{x}{1 + x^2}, \quad (3.69)$$

where $e = \sqrt{1 - \nu^{2/3}}$.

We will assume that $0.65 < \nu \leq 1$. There are two reasons for this assumption. Firstly, we computed Hansen's coefficients up to the 20th order in e , which imposes the limitation $\nu > 0.65$. The second reason is that we will assume $\frac{T_1}{\tau_2} \ll T_1\nu$. This inequality, combined with $|\epsilon|\tau_2 < 1$ and $|x| < 2$, implies that for $k \neq k_*$, $(k - k_*)T_1\nu - \frac{T_1}{\tau_2}x \approx (k - k_*)T_1\nu$. Therefore, equation (3.69) can be approximated by

$$\sum_{k \neq k_*} \frac{\left(X_k^{-3,2}(e) \right)^2}{\left(X_{k_*}^{-3,2}(e) \right)^2} \frac{((k - k_*)T_1\nu)}{1 + \left((k - k_*)T_1\nu \right)^2} = \frac{1 - h_1}{h_1} \frac{x}{1 + x^2}, \quad (3.70)$$

where the term $\frac{\tau_1 x}{1 + \left(\frac{\tau_1 x}{\tau_2}\right)^2}$, corresponding to $k = k_*$, was neglected because $\left|\frac{\tau_1 x}{\tau_2}\right|$ is small.

The function on the right-hand side of equation (3.70) depends solely on x and, except for the factor $\frac{1-h_1}{h_1}$, it is plotted in Figure 11. The function on the left-hand side of equation (3.70) depends only on ν and T_1 . For $k_* = 4$, which corresponds to the resonance $2n - \omega = 0$, this graph with $T_1 = 0.512$ is plotted in Figure 12.

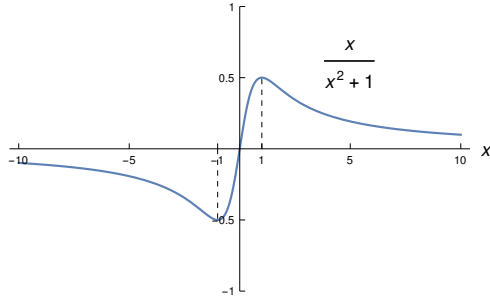


Fig. 11: The function on the right-hand side of equation (3.70).

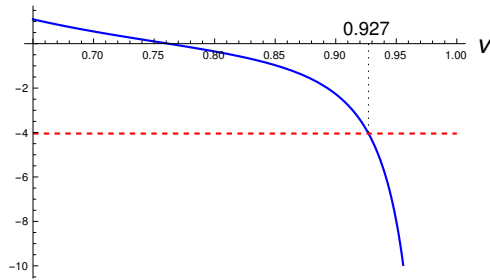


Fig. 12: Graph (solid blue curve) of the function on the left-hand side of equation (3.70) for $T_1 = 0.512$, which corresponds to $\tau_1 n_{mer} = 0.48$. The horizontal line (brown-dashed) corresponds to $-4.045 = -\frac{1-h_1}{2h_1}$, $h_1 = 0.11$.

The function on the right-hand side of equation (3.70) has its minimum equal to $-\frac{1-h_1}{2h_1}$ and its maximum equal to $\frac{1-h_1}{2h_1}$. For a given value of $h_1 \in (0, 1)$, the maximum value of ν on the torque-free curve is determined by the intersection of the horizontal line $-\frac{1-h_1}{2h_1}$ and the graph of the function on the left-hand side of equation (3.70), as depicted in Figure 12. This result should be accurate in the limit as $\tau_2 \rightarrow +\infty$ and is likely reasonable for $\tau_2/\tau_1 \gg 1$.

Using Figure 12, we estimated that on the torque-free curve, close to the resonance $2n - \omega = 0$, and for $T_1 = 0.512$ (which corresponds to $\tau_1 n_{\text{mer}} = 0.48$), ν attains a maximum value of 0.927077. This value is close to 0.9267, which is the value for the corresponding point in Figure 6, where $\frac{T_2}{T_1} = 2900$.

Acknowledgements

L. R. S. is supported in part by FAPEMIG (Fundação de Amparo à Pesquisa no Estado de Minas Gerais) under Grants No. RED-00133-21 and APQ-02153-23.

References

- ME Alexander. The weak friction approximation and tidal evolution in close binary systems. *Astrophysics and Space Science*, 23:459–510, 1973.
- Rose-Marie Baland, Marie Yseboodt, Attilio Rivoldini, and Tim Van Hoolst. Obliquity of Mercury: Influence of the precession of the pericenter and of tides. *Icarus*, 291:136–159, 2017.
- DR Bland. *Linear viscoelasticity*. Pergamon Press, Oxford, 1960.
- Gwenaël Boué and Michael Efroimsky. Tidal evolution of the Keplerian elements. *Celestial Mechanics and Dynamical Astronomy*, 131:1–46, 2019.
- Gwenaël Boué, Alexandre CM Correia, and Jacques Laskar. Complete spin and orbital evolution of close-in bodies using a Maxwell viscoelastic rheology. *Celestial Mechanics and Dynamical Astronomy*, 126(1-3):31–60, 2016.
- Anastasia Consorzi, Daniele Melini, and Giorgio Spada. Relation between the moment of inertia and the k_2 Love number of fluid extra-solar planets. *Astronomy & Astrophysics*, 676:A21, 2023.
- ACM Correia, C Ragazzo, and LS Ruiz. The effects of deformation inertia (kinetic energy) in the orbital and spin evolution of close-in bodies. *Celestial Mechanics and Dynamical Astronomy*, 130(8):51, 2018.
- Alexandre CM Correia and Ema FS Valente. Tidal evolution for any rheological model using a vectorial approach expressed in Hansen coefficients. *Celestial Mechanics and Dynamical Astronomy*, 134(3):24, 2022.
- Alexandre CM Correia, Gwenaël Boué, Jacques Laskar, and Adrián Rodríguez. Deformation and tidal evolution of close-in planets and satellites using a Maxwell viscoelastic rheology. *Astronomy & Astrophysics*, 571:A50, 2014.
- Michael Efroimsky. Bodily tides near spin-orbit resonances. *Celestial Mechanics and Dynamical Astronomy*, 112(3):283–330, 2012.
- Sylvio Ferraz-Mello. Tidal synchronization of close-in satellites and exoplanets. a rheophysical approach. *Celestial Mechanics and Dynamical Astronomy*, 116(2):109–140, 2013.
- Sylvio Ferraz-Mello. Tidal synchronization of close-in satellites and exoplanets: II. Spin dynamics and extension to mercury and exoplanet host stars. *Celestial Mechanics and Dynamical Astronomy*, 122:359–389, 2015.

- Sylvio Ferraz-Mello. Planetary tides: theories. *Satellite Dynamics and Space Missions*, pages 1–50, 2019.
- Sylvio Ferraz-Mello. On tides and exoplanets. *Proceedings of the International Astronomical Union*, 15(S364):20–30, 2021.
- Sylvio Ferraz-Mello, Cristian Beaugé, Hugo A Folonier, and Gabriel O Gomes. Tidal friction in satellites and planets. the new version of the creep tide theory. *The European Physical Journal Special Topics*, 229:1441–1462, 2020.
- Agnès Fienga, Pierre Deram, V Viswanathan, A Ruscio, L Bernus, D Durante, M Gastineau, and J Laskar. *INPOP19a planetary ephemerides*. PhD thesis, IMCCE, 2019.
- HA Folonier, S Ferraz-Mello, and E Andrade-Ines. Tidal synchronization of close-in satellites and exoplanets. III. tidal dissipation revisited and application to Enceladus. *Celestial Mechanics and Dynamical Astronomy*, 130(12):78, 2018.
- Antonio Genova, Sander Goossens, Erwan Mazarico, Frank G Lemoine, Gregory A Neumann, Weijia Kuang, Terence J Sabaka, Steven A Hauck, David E Smith, Sean C Solomon, et al. Geodetic evidence that Mercury has a solid inner core. *Geophysical Research Letters*, 46(7):3625–3633, 2019.
- Yeva Gevorgyan. Homogeneous model for the TRAPPIST-1e planet with an icy layer. *Astronomy & Astrophysics*, 650:A141, June 2021. doi: 10.1051/0004-6361/202140736.
- Yeva Gevorgyan, Gwenaél Boué, Clodoaldo Ragazzo, Lucas S. Ruiz, and Alexandre C.M. Correia. Andrade rheology in time-domain. Application to Enceladus’ dissipation of energy due to forced libration. *Icarus*, 343:113610, 2020.
- Yeva Gevorgyan, Isamu Matsuyama, and Clodoaldo Ragazzo. Equivalence between simple multilayered and homogeneous laboratory-based rheological models in planetary science. *Monthly Notices of the Royal Astronomical Society*, 523(2):1822–1831, 2023.
- Peter Goldreich. Final spin states of planets and satellites. *The Astronomical Journal*, 71:1, 1966.
- Gabriel O Gomes, Hugo A Folonier, and Sylvio Ferraz-Mello. Rotation and figure evolution in the creep tide theory: a new approach and application to Mercury. *Celestial Mechanics and Dynamical Astronomy*, 131(12):56, 2019.
- Sander Goossens, Joe P Renaud, Wade G Henning, Erwan Mazarico, Stefano Bertone, and Antonio Genova. Evaluation of recent measurements of Mercury’s moments of inertia and tides using a comprehensive Markov Chain Monte Carlo method. *The Planetary Science Journal*, 3(2):37, 2022.
- P Hut. Tidal evolution in close binary systems. *Astronomy and Astrophysics*, vol. 99, no. 1, June 1981, p. 126-140., 99:126–140, 1981.
- William M Kaula. Tidal dissipation by solid friction and the resulting orbital evolution. *Reviews of geophysics*, 2(4):661–685, 1964.
- Valeri V Makarov. Conditions of passage and entrapment of terrestrial planets in spin-orbit resonances. *The Astrophysical Journal*, 752(1):73, 2012.
- Valeri V Makarov and Michael Efroimsky. No pseudosynchronous rotation for terrestrial planets and moons. *The Astrophysical Journal*, 764(1):27, 2013.

- Jean-Luc Margot, SA Hauck II, E Mazarico, Stanton J Peale, and Sebastiano Padovan. Mercury's internal structure. *Mercury-The view after MESSENGER*, pages 85–113, 2018.
- I Matsuyama and F Nimmo. Gravity and tectonic patterns of Mercury: Effect of tidal deformation, spin-orbit resonance, nonzero eccentricity, despinning, and reorientation. *Journal of Geophysical Research: Planets*, 114(E1), 2009.
- Isamu Matsuyama, Francis Nimmo, James T Keane, Ngai H Chan, G Jeffrey Taylor, Mark A Wieczorek, Walter S Kiefer, and James G Williams. GRAIL, LLR, and LOLA constraints on the interior structure of the Moon. *Geophysical Research Letters*, 43(16):8365–8375, 2016.
- F Mignard. The evolution of the lunar orbit revisited. I. *The Moon and the planets*, 20(3):301–315, 1979.
- Benoit Noyelles, Julien Frouard, Valeri V Makarov, and Michael Efroimsky. Spin-orbit evolution of Mercury revisited. *Icarus*, 241:26–44, 2014.
- Gordon I Ogilvie. Tidal dissipation in stars and giant planets. *Annual Review of Astronomy and Astrophysics*, 52:171–210, 2014.
- C Ragazzo and L S Ruiz. Spin-orbit synchronization and singular perturbation theory. *To appear*, 2024.
- C Ragazzo and LS Ruiz. Dynamics of an isolated, viscoelastic, self-gravitating body. *Celestial Mechanics and Dynamical Astronomy*, 122(4):303–332, 2015.
- Clodoaldo Ragazzo. The theory of figures of Clairaut with focus on the gravitational modulus: inequalities and an improvement in the Darwin–Radau equation. *São Paulo Journal of Mathematical Sciences*, 14:1–48, 2020.
- Clodoaldo Ragazzo and LS Ruiz. Viscoelastic tides: models for use in Celestial Mechanics. *Celestial Mechanics and Dynamical Astronomy*, 128(1):19–59, 2017.
- Clodoaldo Ragazzo, Gwenaél Boué, Yeva Gevorgyan, and Lucas S Ruiz. Librations of a body composed of a deformable mantle and a fluid core. *Celestial Mechanics and Dynamical Astronomy*, 134(2):10, 2022.
- MG Rochester and DE Smylie. On changes in the trace of the Earth's inertia tensor. *Journal of Geophysical Research*, 79(32):4948–4951, 1974.
- Roberto Sabadini, Bert Vermeersen, and Gabriele Cambiotti. *Global dynamics of the Earth*. Springer, 2016.
- SF Singer. The origin of the Moon and geophysical consequences. *Geophysical Journal International*, 15(1-2):205–226, 1968.
- G Steinbrügge, S Padovan, H Hussmann, T Steinke, A Stark, and J Oberst. Viscoelastic Tides of Mercury and the Determination of its Inner Core Size. *Journal of Geophysical Research: Planets*, 123(10):2760–2772, 2018.